

# Numerical studies of nonlinear ultrasonic guided waves in uniform waveguides with arbitrary cross sections

Cite as: AIP Advances 6, 075207 (2016); <https://doi.org/10.1063/1.4959005>

Submitted: 30 March 2016 • Accepted: 03 July 2016 • Published Online: 13 July 2016

Peng Zuo,  Yu Zhou and  Zheng Fan



View Online



Export Citation



CrossMark

## ARTICLES YOU MAY BE INTERESTED IN

[Numerical and experimental investigation of nonlinear ultrasonic Lamb waves at low frequency](#)

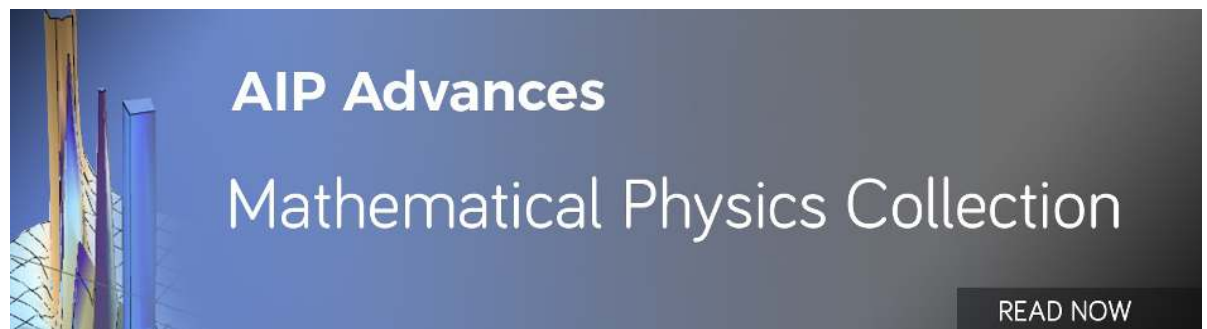
Applied Physics Letters **109**, 021902 (2016); <https://doi.org/10.1063/1.4958705>

[Nonlinear ultrasonic guided waves—Principles for nondestructive evaluation](#)

Journal of Applied Physics **129**, 021101 (2021); <https://doi.org/10.1063/5.0038340>

[Investigation of nonlinear ultrasonic guided waves in open waveguides based on perfectly matched layers](#)

The Journal of the Acoustical Society of America **144**, 1572 (2018); <https://doi.org/10.1121/1.5055210>



AIP Advances  
Mathematical Physics Collection

READ NOW

## Numerical studies of nonlinear ultrasonic guided waves in uniform waveguides with arbitrary cross sections

Peng Zuo,<sup>1</sup> Yu Zhou,<sup>2</sup> and Zheng Fan<sup>1,a</sup>

<sup>1</sup>*School of Mechanical and Aerospace Engineering, Nanyang Technological University, 50 Nanyang Avenue, Singapore 639798, Singapore*

<sup>2</sup>*Advanced Remanufacturing and Technology Center (ARTC), 3 Clean Tech Loop, CleanTech Two, Singapore 637143, Singapore*

(Received 30 March 2016; accepted 3 July 2016; published online 13 July 2016)

Nonlinear guided waves have been investigated widely in simple geometries, such as plates, pipe and shells, where analytical solutions have been developed. This paper extends the application of nonlinear guided waves to waveguides with arbitrary cross sections. The criteria for the existence of nonlinear guided waves were summarized based on the finite deformation theory and nonlinear material properties. Numerical models were developed for the analysis of nonlinear guided waves in complex geometries, including nonlinear Semi-Analytical Finite Element (SAFE) method to identify internal resonant modes in complex waveguides, and Finite Element (FE) models to simulate the nonlinear wave propagation at resonant frequencies. Two examples, an aluminum plate and a steel rectangular bar, were studied using the proposed numerical model, demonstrating the existence of nonlinear guided waves in such structures and the energy transfer from primary to secondary modes. © 2016 Author(s). All article content, except where otherwise noted, is licensed under a Creative Commons Attribution (CC BY) license (<http://creativecommons.org/licenses/by/4.0/>). [<http://dx.doi.org/10.1063/1.4959005>]

### I. INTRODUCTION

Linear ultrasonic methods, widely used in non-destructive evaluation (NDE), are only sensitive to macro-damages in the order of the wavelength of the ultrasound but they are not capable for micro-damages such as micro-cracks or material degradation,<sup>1</sup> which usually occur at very early stage of the operation. Such challenge may be overcome by using nonlinear ultrasonic methods, as they are much more sensitive to incipient damages.<sup>2-5</sup> In recent years, nonlinear ultrasonic guided waves, combining advantages of nonlinear ultrasound and guided waves, have emerged as a useful tool for the characterization of incipient damages in large structures, as guided waves can travel a long distance with little loss in energy and therefore provide capability for the remote inspection of areas with difficult access.<sup>5</sup>

The theory of nonlinear guided waves was first demonstrated in 1990s by Deng.<sup>6,7</sup> Two conditions for the generation of the cumulative second harmonic wave were summarized using perturbation method and modal analysis: (1) phase velocity matching; (2) non-zero power transfer from the primary to the second harmonic wave.<sup>8</sup> Müller *et al.*<sup>9</sup> obtained analytical asymptotic solutions to Lamb waves and five mode types for the cumulative increase in the amplitude of the second harmonic wave with the propagation distance. The theoretical analysis was extended from plate like structures to cylindrical rod and pipe structures by de Lima *et al.*<sup>10</sup> and Chillara *et al.*<sup>11</sup> More recently, Liu *et al.* demonstrated a method for the selection of primary modes with respect to the internal resonance,<sup>12</sup> also extended the work to higher order harmonics.<sup>13-15</sup>

Following theoretical analysis, a number of applications have been developed using nonlinear guided waves, including characterization of material nonlinearity in elastic plates using Lamb

---

<sup>a</sup>Electronic mail: [ZFAN@ntu.edu.sg](mailto:ZFAN@ntu.edu.sg)

waves,<sup>16–18</sup> evaluation of incipient damages (creep,<sup>19</sup> fatigue<sup>20–22</sup> and plasticity<sup>23,24</sup>) in plate like structures, investigation of the material decay,<sup>25,26</sup> as well as assessment of thermal fatigue damages in isotropic pipes.<sup>27</sup>

However, most studies on nonlinear ultrasonic guided waves are limited to simple geometries, such as plates, rods or pipes. More recently, nonlinear SAFE algorithms were proposed<sup>28,29</sup> for waveguides with arbitrary cross section to analyze modal properties and nonlinear internal resonant conditions, for the application to measure the neutral temperature in railway structures.<sup>30</sup> It is known that experimental investigation of nonlinear guided waves is very challenging due to weak harmonic waves, noise, and the system nonlinearity. Therefore in order to further explore nonlinear guided waves in various waveguides, it is important to develop a numerical framework that is capable to compute resonant modes in complex waveguides efficiently, and simulate the propagation of nonlinear guided waves using optimized generation and signal processing methods.

The paper starts with a review of the theory of nonlinear ultrasonic guided waves, following by the introduction of the numerical framework to predict the internal resonant modes in a complex waveguide using an improved nonlinear SAFE algorithm, and time domain FE simulations to confirm the existence of internal resonant modes and validate their properties. The numerical models were first demonstrated in an aluminum plate which can be compared with analytical solutions, and then they were applied on a rectangular steel bar which can only be analyzed by numerical methods.

## II. MATHEMATICAL FRAMEWORK OF NONLINEAR ULTRASONIC GUIDED WAVES

In this section, a brief review of generalized nonlinear elasticity wave propagation theory using finite deformations and nonlinear material properties is presented. To describe the finite deformation, a set of markers, with coordinates  $\mathbf{X}$  in the reference configuration are attached to these material particles. At time  $t$ , the material particles move to new positions in the current configuration and is written as  $\mathbf{x} = \varphi(\mathbf{X}, t)$ . The change in shape of infinitesimal volume elements within the solid can be characterized by the deformation gradient tensor,

$$\mathbf{F} = \frac{\partial \mathbf{x}}{\partial \mathbf{X}}. \quad (1)$$

The Green-Lagrange strain tensor is defined in terms of the deformation gradient tensor

$$\mathbf{E} = \frac{1}{2} (\mathbf{F}^T \mathbf{F} - \mathbf{I}), \quad (2)$$

where  $\mathbf{F}^T$  represents transposition of  $\mathbf{F}$ , and  $\mathbf{I}$  represents the identity tensor. To describe the nonlinear material properties, Landau-Lifshitz hyperelastic constitutive model is given through a strain energy density function including third order elastic constants

$$w = \frac{1}{2} \lambda I_1^2 + \mu I_2 + \frac{1}{3} C I_1^3 + B I_1 I_2 + \frac{1}{3} A I_3, \quad (3)$$

where  $\lambda$  and  $\mu$  are Lamé constants;  $A$ ,  $B$  and  $C$  are third order elastic constants;  $I_1$ ,  $I_2$  and  $I_3$  are defined by  $I_1 = E_{ii}$ ,  $I_2 = E_{ij} E_{ji}$  and  $I_3 = E_{ij} E_{jk} E_{ki}$ , representing the first three invariants of the Green-Lagrange tensor. Basing on the first Piola-Kirchhoff (P-K) stress tensor, the momentum equation describing the dynamic behavior of the solid is given in the reference configuration by

$$\rho_0 \ddot{\mathbf{u}} = \nabla \cdot \mathbf{s}, \quad (4)$$

where  $\rho_0$  is the density of the material in the reference configuration,  $\mathbf{u}$  is the displacement and  $\nabla$  is the gradient operator with respect to the reference configuration. The second P-K stress tensor is given by

$$\mathbf{S} = \frac{\partial w}{\partial \mathbf{E}}. \quad (5)$$

The first P-K stress is related to the second P-K stress by

$$\mathbf{s} = \mathbf{F}\mathbf{S}. \quad (6)$$

Eqs. (2) and (4)-(6) are the set of governing equations describing the wave propagation in solids. For simplicity, combining Eqs. (2) and (4)-(6), the governing equations with stress free boundary condition can be formulated as a concise form in terms of the displacement  $\mathbf{u}$ ,

$$\rho_0 \ddot{\mathbf{u}} = (\lambda + 2\mu) \nabla (\nabla \cdot \mathbf{u}) - \mu \nabla \times (\nabla \times \mathbf{u}) + \bar{\mathbf{f}}, \quad (7)$$

$$(\mathbf{s}_L(\mathbf{u}) - \bar{\mathbf{s}}(\mathbf{u})) \cdot \mathbf{n}_r = \mathbf{0}, \quad (8)$$

where  $\mathbf{n}_r$  is a unit vector normal to the surface of the solids and  $\mathbf{s}_L(\mathbf{u})$  is the corresponding linear part of the first P-K stress tensor, which is given by

$$\mathbf{s}_L(\mathbf{u}) = \frac{\lambda}{2} (\nabla \mathbf{u} + \nabla^T \mathbf{u}) \mathbf{I} + \mu (\nabla \mathbf{u} + \nabla^T \mathbf{u}). \quad (9)$$

$\bar{\mathbf{f}}$  and  $\bar{\mathbf{s}}(\mathbf{u})$  represent nonlinear terms and they can be explicitly expressed using tensor components as

$$\begin{aligned} \bar{f}_i &= \left( \mu + \frac{A}{4} \right) (u_{l,kk} u_{l,i} + u_{l,kk} u_{i,l} + 2u_{i,lk} u_{l,k}) + \left( \lambda + \mu + \frac{A}{4} + B \right) \\ &\times (u_{l,ik} u_{l,k} + u_{k,lk} u_{i,l}) + (\lambda + B) (u_{i,kk} u_{l,l}) + \left( \frac{A}{4} + B \right) \\ &\times (u_{k,lk} u_{l,i} + u_{k,ik} u_{k,l}) + (B + 2C) (u_{k,ik} u_{l,l}) + O(u_i^3), \end{aligned} \quad (10)$$

$$\begin{aligned} \bar{s}_{ij} &= \left( \frac{\lambda}{2} u_{k,l} u_{k,l} + C u_{k,k} u_{l,l} \right) \delta_{ij} + B u_{k,k} u_{j,i} + \frac{A}{4} u_{j,k} u_{k,i} \\ &+ \frac{B}{2} (u_{k,l} u_{k,l} + u_{k,l} u_{l,k}) \delta_{ij} + (\lambda + B) u_{k,k} u_{i,j} \\ &+ \left( \mu + \frac{A}{4} \right) (u_{i,k} u_{j,k} + u_{k,i} u_{k,j} + u_{i,k} u_{k,j}) + O(u_i^3), \end{aligned} \quad (11)$$

where  $\delta_{ij}$  is the Kronecker delta,  $O(u_i^3)$  is the higher order term.

This nonlinear wave propagation equation can be solved by using the perturbation theory in which the displacement field  $\mathbf{u}$  is expressed as<sup>10</sup>

$$\mathbf{u} = \mathbf{u}^{(1)} + \mathbf{u}^{(2)}, \quad (12)$$

where  $\mathbf{u}^{(1)}$  is the primary displacement field, and  $\mathbf{u}^{(2)}$  is the secondary displacement field, which is very small compared with  $\mathbf{u}^{(1)}$ . Combining Eqs. (7), (8) and (12), the nonlinear boundary value problem is divided into two linear boundary value problems. In the first-order approximation, the governing equation and boundary condition are given by

$$\rho_0 \ddot{\mathbf{u}}^{(1)} = (\lambda + 2\mu) \nabla (\nabla \cdot \mathbf{u}^{(1)}) - \mu \nabla \times (\nabla \times \mathbf{u}^{(1)}), \quad (13)$$

$$\mathbf{s}_L(\mathbf{u}^{(1)}) \cdot \mathbf{n}_r = \mathbf{0}, \quad (14)$$

where  $\mathbf{s}_L(\mathbf{u}^{(1)})$  is given in terms of  $\mathbf{u}^{(1)}$ . In the second order approximation,

$$\rho_0 \ddot{\mathbf{u}}^{(2)} = (\lambda + 2\mu) \nabla (\nabla \cdot \mathbf{u}^{(2)}) - \mu \nabla \times (\nabla \times \mathbf{u}^{(2)}) + \bar{\mathbf{f}}^{(1)}, \quad (15)$$

$$\mathbf{s}_L(\mathbf{u}^{(2)}) \cdot \mathbf{n}_r = -\bar{\mathbf{s}}^{(1)} \cdot \mathbf{n}_r, \quad (16)$$

where  $\bar{\mathbf{f}}^{(1)}$  and  $\bar{\mathbf{s}}^{(1)}$  are the function of  $\mathbf{u}^{(1)}$ . Once the solution  $\mathbf{u}^{(1)}$  is known, the terms  $\bar{\mathbf{f}}^{(1)}$  and  $\bar{\mathbf{s}}^{(1)}$  are determined by substituting  $\mathbf{u}^{(1)}$  into Eqs. (10) and (11). The solution  $\mathbf{u}^{(2)}$  can be interpreted as a solution with an external force applied in the volume  $\bar{\mathbf{f}}^{(1)}$ , and on the boundary  $\bar{\mathbf{s}}^{(1)}$ . Hence, the original problem reduces to seek two separate solutions.

For the guide wave problem, the appropriate solution form for the primary wave field can be written as

$$\mathbf{u}^{(1)}(x, y, z, t) = \mathbf{U}^{(1)}(x, y) e^{I(kz - \omega t)}, \quad (17)$$

where  $z$  is the direction of the wave propagation and  $\mathbf{U}^{(1)}$  is the displacement in the cross section;  $k$  is the wavenumber;  $\omega = 2\pi f$  is the circular frequency and  $f$  being the frequency. For the primary wave field, the solution can be obtained analytically for simple geometries (plates, rods and shells)<sup>31</sup> and numerically for waveguides with complex geometries.<sup>32</sup> Once the primary wave field is known, the second wave field can be obtained by solving the inhomogeneous system of linear partial differential equation. The second wave field obtained via modal expansion and a reciprocity relation can be written as<sup>33</sup>

$$\mathbf{v}^{(2)}(x, y, z, t) = \frac{1}{2} \sum_{m=1}^{\infty} A_m(z) \mathbf{v}_m^{(2)}(x, y) e^{-i2\omega t} + c.c., \quad (18)$$

where  $\mathbf{v}_m$  and  $A_m$  are the particle velocity vector and the modal amplitude for the  $m$ th mode at  $2\omega$  respectively and  $c.c.$  represents the complex conjugates.  $A_m$  is to quantify the contribution of the  $m$ th mode in the mode expansion, and it is given by

$$A_m(z) = \bar{A}_m(z) e^{i(2kz)} - \bar{A}_m(0) e^{ik_n^* z}, \quad (19)$$

where  $k_n^*$  is the complex conjugate of the wave number of the  $n$ th mode at  $2\omega$ .  $\bar{A}_m$  can be expressed by the following forms.

$$\begin{aligned} \bar{A}_m(z) &= i \frac{(f_n^{\text{vol}} + f_n^{\text{surf}})^*}{4P_{mn}(k_n^* - 2k)} \quad \text{if } k_n^* \neq 2k \text{ (asynchronism)}, \\ \bar{A}_m(z) &= \frac{(f_n^{\text{vol}} + f_n^{\text{surf}})^*}{4P_{mn}} z \quad \text{if } k_n^* = 2k \text{ (synchronism)}, \end{aligned} \quad (20)$$

where  $P_{mn}$  is the complex power flux along the wave propagation direction  $z$ , and the terms  $f_n^{\text{vol}}$  and  $f_n^{\text{surf}}$  represent the power flux through the volume and through the surface of the waveguide, respectively. They are given by

$$\begin{aligned} P_{mn} &= -\frac{1}{4} \int_{\Omega} (\mathbf{v}_n^* \cdot \mathbf{s}_m + \mathbf{v}_m \cdot \mathbf{s}_n^*) \cdot \mathbf{n}_z d\Omega, \\ f_n^{\text{vol}}(z) &= \int_{\Omega} \mathbf{v}_n^* \cdot \bar{\mathbf{f}} d\Omega, \\ f_n^{\text{surf}}(z) &= \int_{\Gamma} \mathbf{v}_n^* \cdot \bar{\mathbf{s}} \cdot \mathbf{n}_r d\Gamma, \end{aligned} \quad (21)$$

where  $\Omega$  and  $\Gamma$  are the cross-sectional area and the surface of the waveguide, respectively;  $\mathbf{n}_z$  is the unit vector in the direction of wave propagation;  $\mathbf{s}_m$  and  $\mathbf{v}_m$  are the first P-K stress tensor and the particle velocity for the  $m$ th mode at  $2\omega$ , respectively.

From Eq. (20), it is evident that the modal amplitude of the generic  $m$ th secondary mode increases with the propagation distance  $z$  if the solution is synchronous. This is known as the internal resonance which relies on two conditions: (1) phase velocity matching:  $k_n^* = 2k$ ; (2) nonzero power transfer from the primary to the secondary wave field:  $f_n^{\text{surf}} + f_n^{\text{vol}} \neq 0$ . As a result, nonlinear guided waves only exist in particular frequencies.

### III. NUMERICAL METHODS

#### A. Nonlinear SAFE algorithm

The SAFE method has been developed to investigate the propagation of guide waves along arbitrary cross-sectional geometries, such as railways,<sup>32,34</sup> square rods,<sup>35</sup> grooved plates<sup>36</sup> and

welded plates.<sup>37</sup> This method uses a finite element representation of the cross section of the waveguide, together with a harmonic description along the propagation direction.

The mathematical model of the SAFE method is based on the three dimensional elasticity approach. The displacement vector therefore can be written as

$$u_i(x, y, z, t) = U_i(x, y) e^{l(kz - \omega t)}, \quad (22)$$

where the subscript  $i = 1, 2, 3$ . The differential equations of motion in an elastic domain of mass density  $\rho$  and elastic constants  $C_{ijkl}$  are

$$\sum_{j,k,l=1}^3 \left[ C_{ijkl} \frac{\partial^2 U_j}{\partial x_k \partial x_l} \right] + \rho \omega^2 U_i = 0, \quad (23)$$

where  $x_1 = x$ ,  $x_2 = y$ ,  $x_3 = z$ . Combining Eq. (22) and Eq. (23) and using some intermediary transformations, the differential equations of motion can be written in the following form

$$C_{ijkl} \frac{\partial^2 U_j}{\partial x_k \partial x_l} + I(C_{i3jk} + C_{ikj3}) \frac{\partial (kU_j)}{\partial x_k} - kC_{i3j3} (kU_j) + \rho \omega^2 \delta_{ij} U_j = 0, \quad (24)$$

where  $j = 1, 2, 3$  and  $k, l = 1, 2$ . This equation forms a quadratic eigenvalue problem, where the eigensolutions are the wave numbers  $k$ , and mode shapes of the waveguide at the chosen angular frequency  $\omega$ . Each solution at a chosen frequency will reveal the wavenumbers of all possible modes at that frequency. The dispersion curve can be calculated by repeating the eigenvalue solution over the desired range of frequencies.

As discussed in Section II, the key step in the investigation of nonlinear guided waves is to identify internal resonant mode pairs, in which the amplitude of the second harmonic wave increases cumulatively with the propagation distance. Eqs. (12)-(16) has shown that the nonlinear guided wave problem can be divided into two linear guided wave problems via perturbation theory, which describe the solutions of the primary wave and second harmonic wave, respectively. The nonlinear SAFE algorithm (combining the SAFE method and the nonlinear analysis) can be divided into two stages corresponding to the two conditions in Eq. (20), based on the linear solutions obtained.

In the first stage, the dispersion curves and modal properties of a given waveguide are developed using the SAFE method and all potential internal resonant mode pairs are selected based on the phase velocity matching criterion between the primary and the secondary mode. A simplified method is implemented by plotting the dispersion curve of the second harmonic waves at its half frequency. Therefore, by overlapping the phase velocity dispersion curves of the primary wave, all the intersection points between the two dispersion curves are selected as the potential resonant points (mode pairs) which satisfy the phase velocity matching criterion.

After identifying the potential internal resonant mode pairs, the second stage is to ensure non-zero power transfer from the primary to the secondary mode. In this stage, an integral process according to Eqs. (20), (21) is implemented where mode shapes obtained from the SAFE method are used to calculate the velocity vector and the first P-K stress tensor in Eq. (21). If there is a power transfer from the primary mode to the secondary mode, the modal amplitude for the secondary mode increases cumulatively with propagation distance and these mode pairs are identified as internal resonance.

## B. Time domain FE model

The nonlinear SAFE algorithm has provided modal solutions of nonlinear guided waves in complex structures, including their frequencies and mode shapes. Based on the prediction from the nonlinear SAFE algorithm, time domain FE model is developed to simulate the propagation of the nonlinear guided wave, and the second harmonic wave is collected to validate the internal resonant modes. Comparing with the experimental investigations of nonlinear guided waves, which usually suffer from the noise and the system nonlinearity, FE models can provide accurate control of the

material properties in a noise-free environment and is therefore an ideal tool to validate findings from the nonlinear SAFE algorithm.

In the time domain FE model, the Murnaghan model, that describes the strain energy function of the material is used, and can be express as<sup>5</sup>

$$w = \frac{1}{2}\lambda(\text{tr}(\mathbf{E}))^2 + \mu\text{tr}(\mathbf{E}^2) + \frac{1}{3}(l + 2m)(\text{tr}(\mathbf{E}))^3 - m\text{tr}(\mathbf{E})\left((\text{tr}(\mathbf{E}))^2 - \text{tr}(\mathbf{E}^2)\right) + n\det(\mathbf{E}), \quad (25)$$

where  $l$ ,  $m$  and  $n$  are Murnaghan constants;  $\text{tr}()$  and  $\det()$  denote trace and determinant of the tensor, respectively. This model is equivalent to the Landau-Lifshiz nonlinear hyperelastic constitutive model in the nonlinear SAFE algorithm, and the relations between the third order of elastic constants in Eq. (3) and  $l$ ,  $m$ ,  $n$  are given by

$$l = B + C, m = \frac{1}{2}A + B, n = A. \quad (26)$$

In the present work, both the nonlinear SAFE algorithm and the time domain FE model were carried out in a commercial finite element software package.<sup>38</sup> In the following sections, two examples were studied using the simulation tool discussed above: an aluminum plate which can be compared with analytical solutions, and a steel bar with rectangular cross section which can only be investigated by finite element models.

## IV. APPLICATIONS

### A. Nonlinear guided waves in a plate

In this section, an aluminum plate with thickness of 1 mm was chosen to demonstrate the nonlinear SAFE algorithm and to be compared with analytical solutions. Material properties for the plate are listed in Table I. The behavior of the modal amplitude for the secondary mode was discussed at both resonant and non-resonant frequencies.

Figure 1 presents phase velocity dispersion curves of the aluminum plate, in which primary modes are shown in solid curves with upper case labels while second harmonic modes are plotted in dashed curves with lower case labels at their half frequencies. All intersection points of the two group of curves were identified as potential resonant points, following by the calculation of the energy transfer from the primary mode to the corresponding secondary mode. In Fig. 1, four resonant points were identified from 0 to 500 KHz marked with triangles: namely (SH0, s0) at 1710.2 KHz, (SH1, s1) at 1780.6 KHz, (S1, s2) and (SH2, s2) at 3561.2 KHz. The results agree very well with the ones derived from the theoretical analysis.<sup>12</sup> It can be noted that there are another three intersection points marked with dots, which are (S0, sh1) at 954.3 KHz, (S0, a1) at 2219.6 KHz and (A1, sh3) at 2649.5 KHz, and they correspond to non-resonant points due to zero energy transfer from the primary to the secondary mode.

Table II demonstrates the energy transfer from the primary mode to the secondary mode at all intersection points in Fig. 1. Modal amplitudes with respect to the propagation distance for the secondary modes are listed in the table. For internal resonant points ((SH0, s0), (SH1, s1), (S1, s2), (SH2, S2)), it can be seen that the modal amplitude of the secondary mode increases cumulatively with the propagation distance and the (S1, s2) pair has the highest energy transfer efficiency. For non-resonant points ((S0, sh1), (S0, a1), (A1, sh3)), the amplitude of the second harmonic wave is almost zero along the propagation distance, indicating zero energy transferring from the primary to the secondary mode.

TABLE I. Material properties used in the models.<sup>12,15</sup>

Material	$\rho_0(\text{kg/m}^3)$	$\lambda(\text{GPa})$	$\mu(\text{GPa})$	$A(\text{GPa})$	$B(\text{GPa})$	$C(\text{GPa})$
Aluminium	2700	55.27	25.95	-351.2	-149.4	-102.8
Steel	7932	107.8	84.7	-325	-310	-800

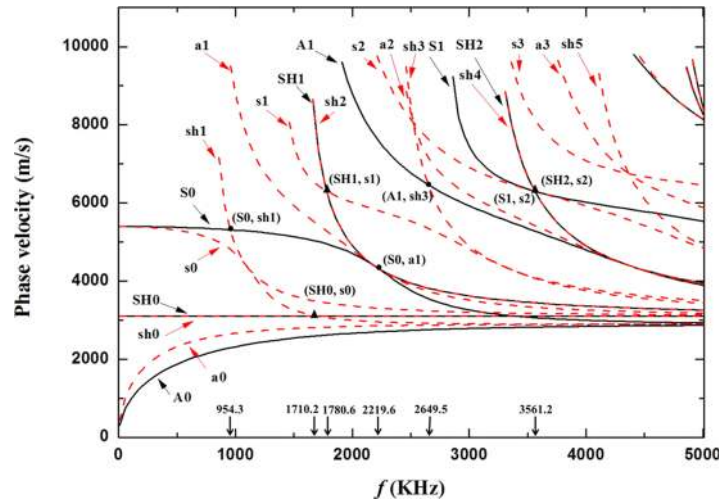


FIG. 1. Phase velocity dispersion curves for RL modes and SH modes in the aluminate plate.

It has been shown that nonlinear guided waves only exist in limited frequency points as it needs to follow two strict criteria. However, in practice, it is not feasible to choose the exact excitation frequency due to the uncertainty of the material properties in experiment. Fig. 2 demonstrates the behavior of the second harmonic wave, when the excitation frequency deviates slightly from the resonant frequency predicted from the nonlinear SAFE algorithm. A deviation factor,  $\delta = (f - f_{\text{resonant}}) / f_{\text{resonant}}$  is used to quantify the difference from the excitation frequency of the resonant mode pair (S1, s2) at 3561.2 KHz. It can be seen from Fig. 2 that when there is a significant deviation the modal amplitude of the second harmonic wave is bounded and oscillates with a specific period, and this period increases when the deviation decreases. Such oscillation phenomenon for the secondary mode has also been mentioned in references.<sup>8,9,39,40</sup> When the deviation is small, the modal amplitude of the second harmonic wave approaches the resonant one. This suggests that in the real experiment, when the exact resonant frequency is not certain, it is still possible to collect the cumulatively increased secondary mode within a limited propagation distance. Such distance decreases with larger mismatch between the excitation and the resonant frequency.

Time domain FE simulation was carried out in this section, using the internal resonant mode pair (S1, s2) at 3561.2 KHz. This pair has been widely investigated among researchers<sup>16–26</sup> for nonlinear guided waves, as both phase and group velocity of the primary mode match with the secondary mode and therefore easier for the signal post processing. The schematic of the plate model used for the simulation is shown in Fig. 3(a). Plane strain condition was applied in the model. The length of the plate was assumed to be 400 mm. Prescribed displacement boundary condition as a input signal was applied at the left end of the plate to excite the primary mode, using a 20

TABLE II. Modal amplitudes (arbitrary unit) of secondary modes with respect to the propagation distance.

mode pair	distance (m)				
	0.1	0.3	0.5	0.7	0.9
(SH0, s0)	2490	7470	12450	17430	22410
(SH1, s1)	244.13	732.39	1220.65	1708.91	2197.17
(S1, s2)	7049	21147	35245	49343	70490
(SH2, s2)	492.11	1476.33	2460.55	3444.77	4428.99
(S0, sh1)	0.0019	0.0056	0.0093	0.0130	0.0168
(S0, a1)	0.0317	0.0928	0.1474	0.1916	0.2223
(A1, sh3)	0.1616	0.4847	0.8079	1.131	1.4541



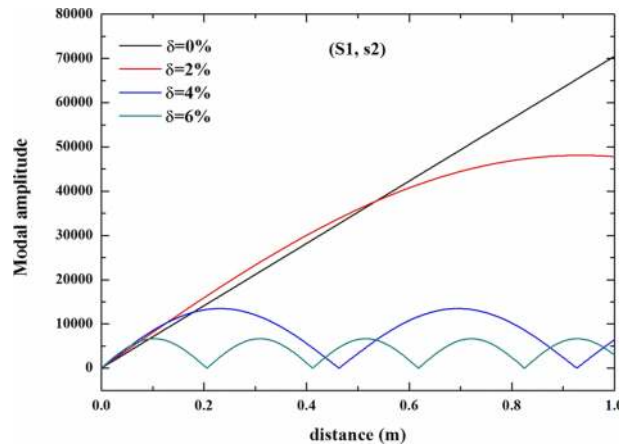


FIG. 2. Behaviors of the modal amplitude (arbitrary unit) for the s2 mode with different deviation from the resonant frequency.

cycle Hanning windowed toneburst with central frequency of 3561.2 KHz. In order to maximize the generation of the primary mode (S1), the input time signal at each specified node at the left end of the plate was scaled according to the mode shape of the primary mode (shown in Fig. 3(b)).<sup>41</sup> Stress free boundary conditions were applied to other boundaries. In the simulation model, rectangular elements were used with a maximum element size of 0.09 mm, and a maximum time step of 0.0025 μs was used. Since both S1 and s2 mode are dominant by the in-plane displacement in the z direction,<sup>31</sup> and the maximum displacement occurs on the surface as shown in Fig. 3(b) and 3(c), the monitor points were placed on the top surface of the plate to pick up the in-plane displacement, at propagation distances from 10 mm to 300 mm in a step of 10 mm.

Figure 4(a) shows received signals monitored at 100 mm away from the generator. S1 and S0 modes at the primary frequency (3561.2 KHz) and s2 mode at the second harmonic frequency (7122.4 KHz) were identified by using frequency domain analysis. Short time Fourier transform (STFT) was used to identify mode properties and resolve the amplitude of specific modes in the

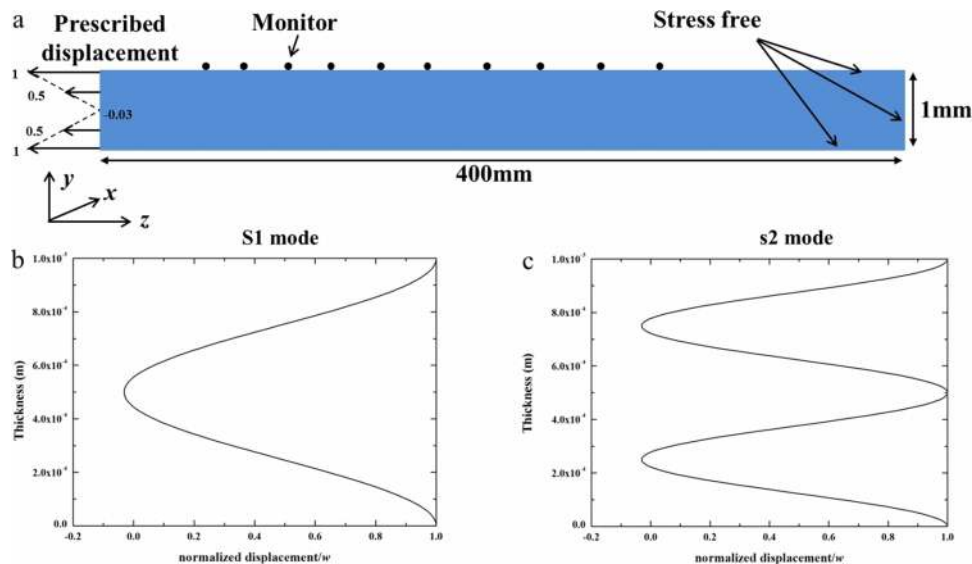


FIG. 3. (a) Schematic of the plate for the finite element simulation, numbers in the left side of the plate are scale factors of the displacement of the node. (b) Displacement in the z direction of the S1 mode at 3561.2 KHz. (c) Displacement in the z direction of the s2 mode at 7122.4 KHz.

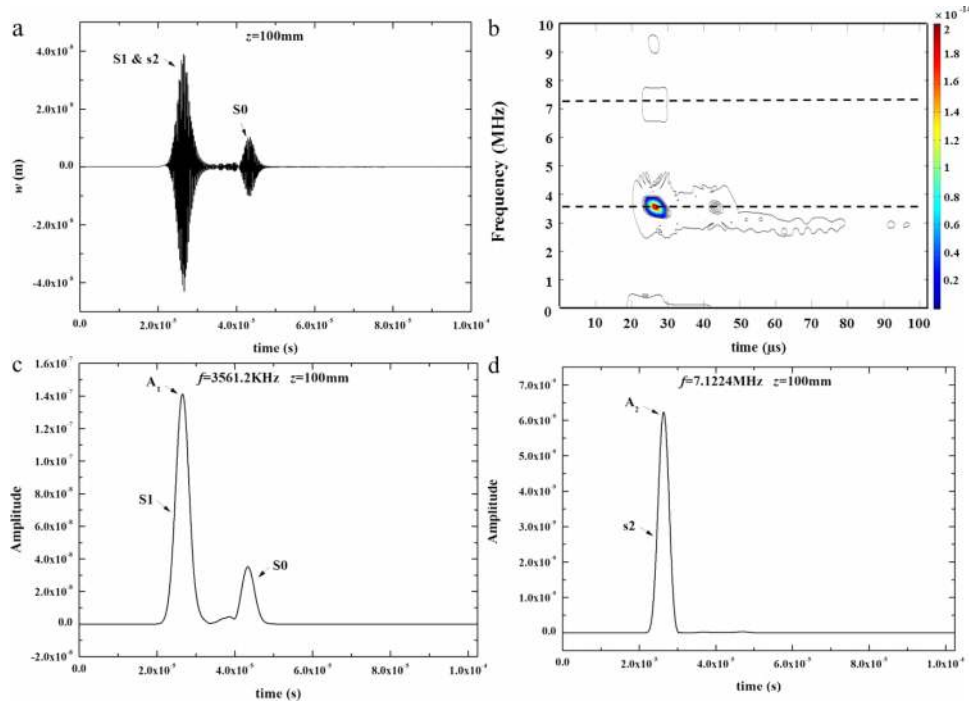


FIG. 4. (a) Time domain signal received at a propagation distance of 100 mm; (b) STFT's of the time domain signal; (c), (d) Slices at the primary and second harmonic frequencies as a function of time.

frequency domain, due to its capability to provide accurate results within a short propagation distance. Fig. 4(b) shows the STFT results of the time domain signal, in which the primary and second harmonic frequencies are marked with dotted horizontal lines. Slices at these two frequencies are shown in Fig. 4(c) and 4(d), respectively. Fig. 4(c) shows received wave packets in the primary frequency. Both S1 and S0 mode were identified, while the S0 mode has slower group velocity and much less amplitude due to the specific excitation method. In Fig. 4(d), only the s2 mode were identified in the frequency of the second harmonic wave. The amplitude of the primary and the secondary mode ( $A_1$  and  $A_2$ ) can be obtained by identifying the maximum value in the corresponding wave packets.

The modal amplitude ratio,  $A_2/A_1^2$ , also named as the relative nonlinear parameter, is plotted with respect to the propagation distance in Fig. 5. It clearly demonstrates that the relative

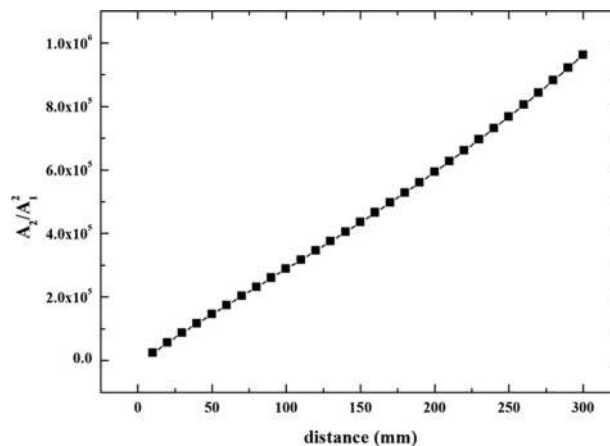


FIG. 5. Relative nonlinear parameter with respect to the propagation distance.

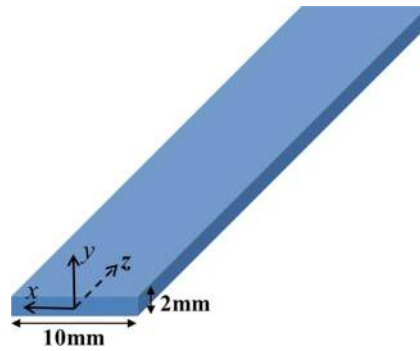


FIG. 6. Schematic of the rectangular bar in the modelling.

nonlinear parameter increases linearly with propagation distance, which confirms that the (S1, s2) pair at 3561.2 kHz is an internal resonant mode pair.

## B. Nonlinear guided waves in a rectangular bar

A steel bar of rectangular cross section with the length of 10 mm and the width of 2 mm was considered in this section. Material properties of steel are listed in Table I. The schematic of the rectangular bar is shown in Fig. 6, with the coordinate shown at the center of the rectangular cross section.

Due to the complex geometry of the cross section, no analytical solution of the primary wave field is available for the bar. However, propagation modes in a rectangular bar have been studied and classified via approximate theories.<sup>42</sup> Due to the twofold symmetry of the rectangular cross section, the modes of wave propagation in rectangular bar can be classified into three categories. (1) Longitudinal modes, in which displacements and stresses are symmetrical with respect to both  $x$  and  $y$  axis. (2) Torsional modes, in which displacements and stresses are asymmetrical with respect to the  $x$  and  $y$  axis, and correspond to a shearing deformation of the bar. In this study, a superscript  $n$  is used to represent the order of the L or the T mode. (3) Bending modes, in which the displacement and the stress are symmetric about either  $x$  axis or  $y$  axis, and asymmetric about the other axis. The bending modes can be classified as  $B_y^n$  and  $B_x^n$ , in which the subscript describes their axis of asymmetry and the superscript denotes their order.

Figure 7 presents the phase velocity dispersion curves for the rectangular bar in 0-500 KHz, including the primary modes in solid line and second harmonic modes (at half frequency) in dashed

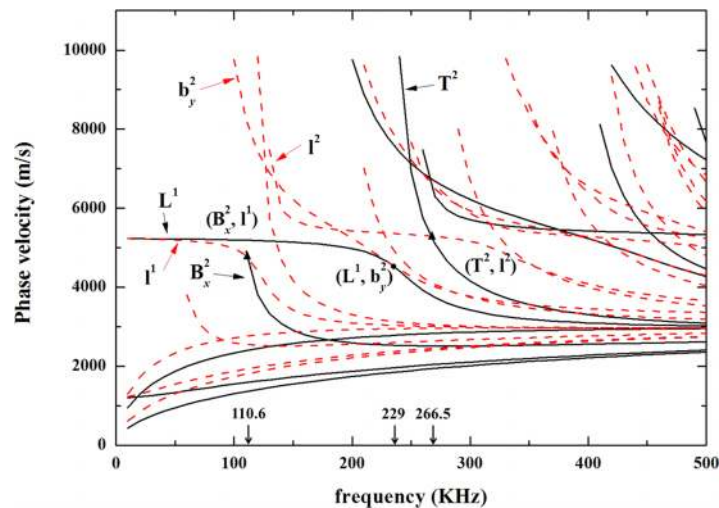


FIG. 7. Phase velocity dispersion curves for the rectangular bar.

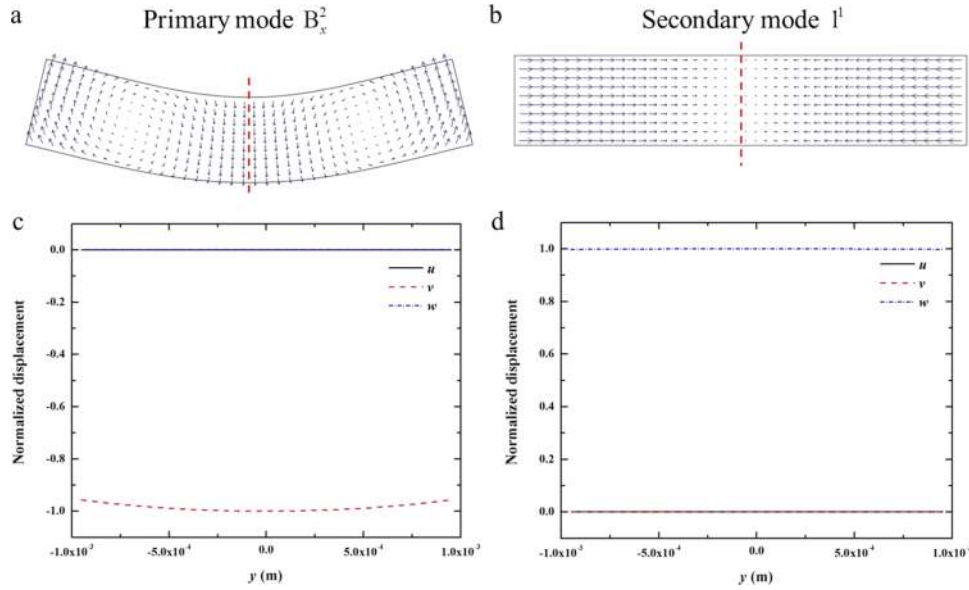


FIG. 8. In-plane displacements (marked as vector arrows) of (a) the primary mode  $B_x^2$  at 110.6 KHz and (b) the secondary mode  $l^1$  at 221.2 KHz. Wave structures of (c) the primary mode and (d) the secondary mode extracted along the cutline, where  $u$ ,  $v$ ,  $w$  represent the normalized displacement in the  $x$ ,  $y$ ,  $z$  direction, respectively.

line. Two internal resonant points were identified and marked with triangles in Fig. 7. They are  $(B_x^2, l^1)$  at the excitation frequency of 110.6 KHz and  $(T^2, l^2)$  at 226.5 KHz, where the upper case letter and lower case letter represent the primary and the secondary mode, respectively. Other intersection points between the solid line and dashed line were identified as non-resonant points as there is no power transfer from the primary to the secondary mode, and one of them,  $(L^1, b_y^2)$  at 229 KHz, was marked in Fig. 7 with black dot as an example.

Figure 8(a) and 8(b) show the mode shapes for the first internal resonant mode pair, the primary mode ( $B_x^2$ ) at 110.6 KHz and the secondary mode ( $l^1$ ) at 221.2 KHz, where the vectors present the in-plane displacement. Fig. 8(c) and 8(d) show the relative displacement in the three axes along a through thickness cutline which bisects the bar. It is observed that the primary mode is dominated by the vertical displacement at the center of the cross section, while the secondary mode is dominated by the axial displacement in the mid-plane of the bar.

Table III presents the distance variation of the modal amplitude of the secondary mode for the three intersection points in Fig. 7. For the internal resonant mode pair,  $(B_x^2, l^1)$  at 110.6 KHz and  $(T^2, l^2)$  at 226.5 KHz, the modal amplitude of the secondary modes increases cumulatively along the propagation distance. For the example of the non-resonant mode pair, i.e.  $(L^1, b_y^2)$  at 229 KHz, the modal amplitude of the secondary mode,  $b_y^2$ , is almost zero, which confirms no energy transferring from the primary to the second mode.

In the FE simulation, the internal resonant mode pair  $(B_x^2, l^1)$  at 110.6 KHz was selected. The schematic of the rectangular bar is shown in Fig. 9(a). The length of the modeled rectangular bar was 3000 mm. In order to maximize the generation of the primary mode, prescribed amplitude which properly matched with the mode shape of the primary mode (Fig. 8(a)), was applied at

TABLE III. Modal amplitudes (arbitrary unit) of secondary modes with respect to the propagation distance.

mode pair	distance (m)				
	0.1	0.3	0.5	0.7	0.9
$(B_x^2, l^1)$	592.85	1778.55	2964.25	4149.95	5335.65
$(T^2, l^2)$	27.84	83.52	139.20	194.88	250.56
$(L^1, b_y^2)$	0.00025	0.00078	0.0013	0.0018	0.0023

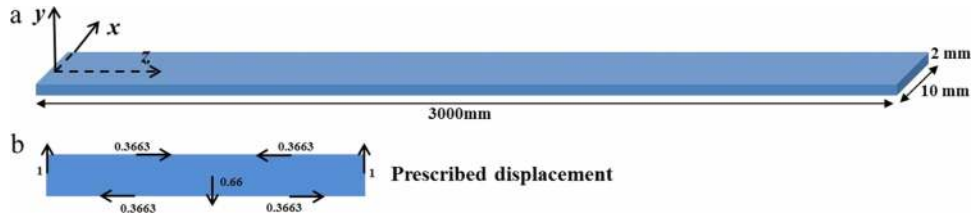


FIG. 9. Schematic of the rectangular bar for the finite element simulation. Numbers in (b) represent the scale factor of the displacement of the node.

specified nodes on the cross section of the bar, as shown in Fig. 9(b). A 20 cycle Hanning windowed tone burst with a central frequency of 110.6 KHZ was used in the simulation. Stress free boundary condition was applied to other boundaries. In the simulation, tetrahedron elements were used with a maximum element size of 2 mm and the maximum time step was 0.1  $\mu$ s. The propagation of the wave was monitored by points in the center of the cross section ( $x = 0, y = 0$ ), from 10 mm to 1000 mm along the  $z$  axis with a step of 10 mm. The displacements in the  $y$  and the  $z$  direction were recorded for the analysis of the primary mode  $B_x^2$  and the secondary mode  $l^1$  respectively, according to their mode shapes.

Figure 10 shows time domain signals obtained for the primary mode ( $v$ ) and the secondary mode ( $w$ ) at 410 mm from the excitation. As illustrated in Fig. 10(a), two modes,  $B_x^1$  and  $B_x^2$ , were generated due to the similarity in their mode shapes, although the amplitude of the  $B_x^2$  mode was significantly larger due to the mode-shape-matching excitation method.

Fig. 10(b) shows the displacement obtained in the  $z$  direction. A number of overlapping wave packets were found in the time domain. In order to identify these modes, the mode shape along the  $z$  direction of both primary and secondary modes are analyzed in Fig. 11. It can be seen from Fig. 11(a) that the excited two primary modes,  $B_x^1$  and  $B_x^2$ , have no displacement in the middle of the bar. Fig. 11(b) demonstrates that among all possible secondary modes, only  $l^1$  mode has displacement in the middle of the bar. Therefore it can be confirmed that the packets received at the monitor points is the  $l^1$  mode. It should be noted that although the phase velocities of the  $B_x^2$  and the  $l^1$  mode match with each other as indicated from the nonlinear SAFE algorithm, the group velocities of the two modes do not match. Therefore the received second harmonic wave appears to have a number of wave packets overlapping with each other. Such phenomenon has also been reported by Deng *et al.*<sup>43</sup> In order to analyze the nonlinearity of the wave, the integrated amplitude of the second harmonic wave need to be used, and therefore fast Fourier transform (FFT) was applied for the signal processing instead of STFT method.

Since the wave packets of the two bending modes start to separate completely at the propagation distance of 410 mm, signals were obtained between 410 mm and 810 mm for post processing. Fig. 12 shows the relative nonlinear parameter  $A_2/A_1^2$ , in which  $A_1$  and  $A_2$  are amplitudes of the

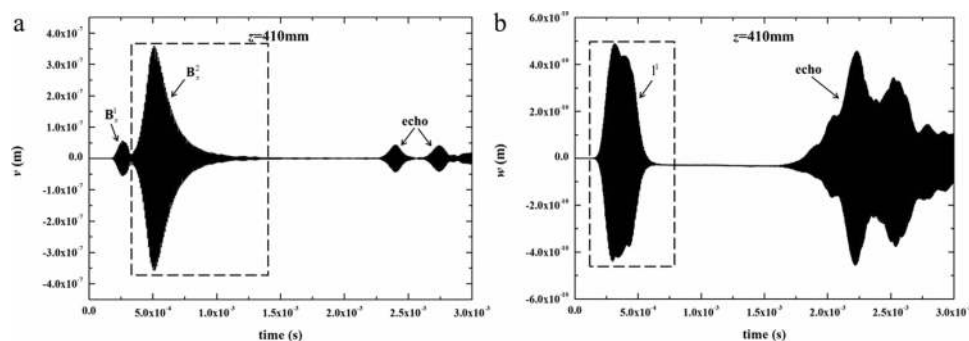


FIG. 10. Time domain signals for (a) out of plane displacement of the primary mode and (b) in-plane displacement of the secondary mode received at a propagation distance of 410 mm.

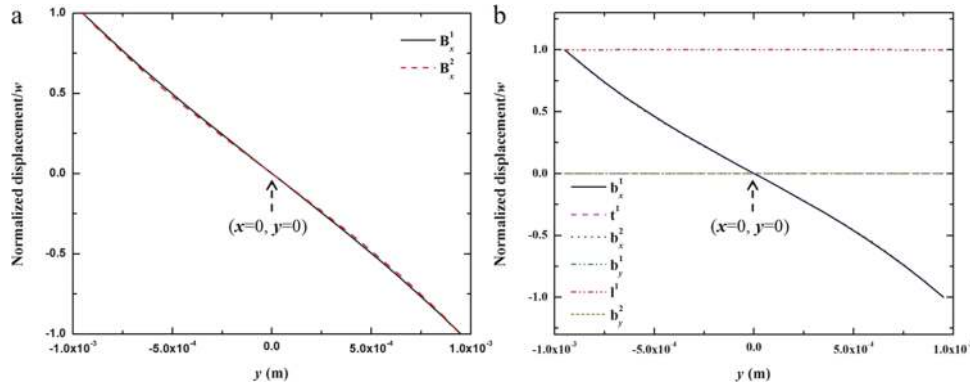


FIG. 11. Displacement component in the  $z$  direction for (a) the primary mode at 110.6 KHz and (b) the secondary modes at 221.2 KHz.

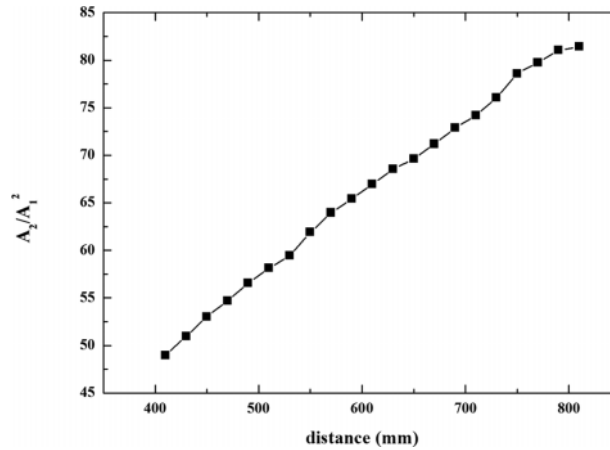


FIG. 12. Relative nonlinear parameter with respect to the propagation distance for the excitation of the  $B_x^2$  mode.

dominant displacement of the primary and the secondary mode. Almost linear increase of the relative nonlinear parameter can be observed, confirming that  $(B_x^2, 1^1)$  at 110.6 kHz is an internal resonant mode pair.

## V. CONCLUSIONS

In this paper, numerical models have been developed to investigate nonlinear guided waves in waveguides with arbitrary cross sections. It has been shown that nonlinear guided waves only exist at particular internal resonant frequencies where the phase velocities of the primary and second harmonic modes match with each other, and with non-zero energy transferring from the former to the latter. The nonlinear SAFE algorithm was used for the modal study of the complex waveguide, and resonant frequencies were identified from the calculation of dispersion curves and the power flux in the propagation direction. With the results from the nonlinear SAFE algorithm, FE simulations were performed at the resonant frequencies using the particular mode shapes of the primary mode.

The numerical models were first demonstrated in an aluminum plate, and the predicted internal resonant frequencies were compared with results from analytical solutions, showing perfect agreement. The models were then applied to a steel rectangular bar, which is chosen to represent complex waveguides in general. FE simulations in both cases have clearly shown the accumulative increase of the amplitude of the second harmonic wave with respect to the propagation distance, indicating the strong nonlinearity at internal resonant frequencies.

## ACKNOWLEDGEMENTS

This work was supported by the Singapore Maritime Institute under SMI Simulation & Modeling R&D Programme. The authors would like to thank Dr. Yang Liu from Schlumberger-Doll Research for helpful discussions.

- <sup>1</sup> A. S. Birks and R. E. Green, *Nondestructive testing handbook* (American Society for Nondestructive Testing, Columbus, OH, 1991), Vol. 7.
- <sup>2</sup> Y. P. Zheng, R. G. Maev, and I. Y. Solodov, *Can. J. Phys.* **77**, 927 (2000).
- <sup>3</sup> K. Y. Jhang, *Int. J. Precis. Eng. Man.* **10**, 123 (2009).
- <sup>4</sup> K. H. Matlack, J. Y. Kim, L. J. Jacobs, and J. M. Qu, *J. Nondestruct. Eval.* **34**, 1 (2015).
- <sup>5</sup> V. K. Chillara and C. J. Lissenden, *Opt. Eng.* **55**, 011002 (2016).
- <sup>6</sup> M. X. Deng, *J. Appl. Phys.* **84**, 3500 (1998).
- <sup>7</sup> M. X. Deng, *J. Appl. Phys.* **85**, 3051 (1999).
- <sup>8</sup> W. J. N. de Lima and M. F. Hamilton, *J. Sound Vib.* **265**, 819 (2003).
- <sup>9</sup> M. F. Müller, J. Y. Kim, J. M. Qu, and L. J. Jacobs, *J. Acoust. Soc. Am.* **127**, 2141 (2010).
- <sup>10</sup> W. J. N. de Lima and M. F. Hamilton, *Wave Motion* **41**, 1 (2005).
- <sup>11</sup> V. K. Chillara and C. J. Lissenden, *Ultrasonics* **53**, 862 (2013).
- <sup>12</sup> Y. Liu, V. K. Chillara, and C. J. Lissenden, *J. Sound Vib.* **332**, 4517 (2013).
- <sup>13</sup> Y. Liu, V. K. Chillara, C. J. Lissenden, and J. L. Rose, *J. Appl. Phys.* **114**, 114908 (2013).
- <sup>14</sup> Y. Liu, C. J. Lissenden, and J. L. Rose, *J. Appl. Phys.* **115**, 214901 (2014).
- <sup>15</sup> Y. Liu, C. J. Lissenden, and J. L. Rose, *J. Appl. Phys.* **115**, 214902 (2014).
- <sup>16</sup> M. X. Deng, P. Wang, and X. F. Lv, *J. Phys. D: Appl. Phys.* **38**, 344 (2005).
- <sup>17</sup> C. Bermes, J. Y. Kim, J. M. Qu, and L. J. Jacobs, *Appl. Phys. Lett.* **90**, 021901 (2007).
- <sup>18</sup> C. Bermes, J. Y. Kim, J. M. Qu, and L. J. Jacobs, *Mech. Syst. Signal Pr.* **22**, 638 (2008).
- <sup>19</sup> Y. X. Xiang, M. X. Deng, F. Z. Xuan, and C. J. Liu, *J. Appl. Phys.* **111**, 104905 (2012).
- <sup>20</sup> M. X. Deng and J. F. Pei, *Appl. Phys. Lett.* **90**, 121902 (2007).
- <sup>21</sup> C. Pruell, J. Y. Kim, J. M. Qu, and L. J. Jacobs, *Smart Mater. Struct.* **18**, 035003 (2009).
- <sup>22</sup> W. B. Li, Y. Cho, and J. D. Achenbach, *Smart Mater. Struct.* **21**, 085019 (2012).
- <sup>23</sup> C. Pruell, J. Y. Kim, J. M. Qu, and L. J. Jacobs, *Appl. Phys. Lett.* **91**, 231911 (2007).
- <sup>24</sup> C. Pruell, J. Y. Kim, J. M. Qu, and L. J. Jacobs, *NDT & E Int.* **42**, 199 (2009).
- <sup>25</sup> Y. X. Xiang, M. X. Deng, F. Z. Xuan, and C. J. Liu, *NDT & E Int.* **44**, 768 (2011).
- <sup>26</sup> Y. X. Xiang, M. X. Deng, F. Z. Xuan, and C. J. Liu, *Ultrasonics* **51**, 974 (2011).
- <sup>27</sup> W. Li and Y. Cho, *Exp. Mech.* **54**, 1309 (2014).
- <sup>28</sup> C. Nucera and F. L. di Scalea, *Math. Probl. Eng.* **2012**, 16 pages (2012).
- <sup>29</sup> C. Nucera and F. L. di Scalea, *J. Eng. Mech.* **140**, 502 (2014).
- <sup>30</sup> C. Nucera and F. L. di Scalea, *J. Acoust. Soc. Am.* **136**, 2561 (2014).
- <sup>31</sup> K. F. Graff, *Wave motion in elastic solids* (Courier Corporation, 2012).
- <sup>32</sup> L. Gavrić, *J. Sound Vib.* **185**, 531 (1995).
- <sup>33</sup> B. A. Auld, *Acoustic fields and waves in solids* (R. E. Krieger, 1990), Vol. 2.
- <sup>34</sup> T. Hayashi, W. J. Song, and J. L. Rose, *Ultrasonics* **41**, 175 (2003).
- <sup>35</sup> T. Hayashi, C. Tamayama, and M. Murase, *Ultrasonics* **44**, 17 (2006).
- <sup>36</sup> M. V. Predoi, M. Castaings, B. Hosten, and C. Bacon, *J. Acoust. Soc. Am.* **121**, 1935 (2007).
- <sup>37</sup> Z. Fan and M. J. S. Lowe, *P. Roy. Soc. A-Math. Phy.* **465**, 2053 (2009).
- <sup>38</sup> COMSOL, User's Guide and Introduction (Version 4.4 by COMSOL MULTIPHYSICS, <http://www.comsol.com/>, most recently viewed 20th December 2015).
- <sup>39</sup> Y. X. Xiang, M. X. Deng, and F. Z. Xuan, *J. Appl. Phys.* **106**, 024902 (2009).
- <sup>40</sup> N. Matsuda and S. Biwa, *J. Nondestruct. Eval.* **33**, 169 (2014).
- <sup>41</sup> B. Pavlakovic, D. Alleyne, M. J. S. Lowe, and P. Cawley, in *Review of Progress in Quantitative Nondestructive Evaluation*, edited by D. Thompson and D. Chimenti (Springer, 1998), Vol. 17, pp. 1003–1010.
- <sup>42</sup> W. B. Fraser, *Int. J. Solids Struct.* **5**, 379 (1969).
- <sup>43</sup> M. X. Deng, Y. X. Xiang, and L. B. Liu, *J. Appl. Phys.* **109**, 113525 (2011).